5-2018

Characterization and Analysis of Ultrathin CIGS Films and Solar Cells Deposited by 3-Stage Process

Grace Rajan
Old Dominion University

Krishna Aryal
Old Dominion University

Shankar Karki
Old Dominion University

Puruswottam Aryal

Robert W. Collins

See next page for additional authors

Authors

Grace Rajan, Krishna Aryal, Shankar Karki, Puruswottam Aryal, Robert W. Collins, and Sylvain Marsillac

Research Article

Characterization and Analysis of Ultrathin CIGS Films and Solar Cells Deposited by 3-Stage Process

Grace Rajan,[1] Krishna Aryal,[1] Shankar Karki,[1] Puruswottam Aryal,[2] Robert W. Collins,[2] and Sylvain Marsillac [1]

[1]*Virginia Institute of Photovoltaics, Old Dominion University, Norfolk, VA 23529, USA*
[2]*Department of Physics & Astronomy, University of Toledo, Toledo, OH 43606, USA*

Correspondence should be addressed to Sylvain Marsillac; smarsill@odu.edu

In view of the large-scale utilization of $Cu(In,Ga)Se_2$ (CIGS) solar cells for photovoltaic application, it is of interest not only to enhance the conversion efficiency but also to reduce the thickness of the CIGS absorber layer in order to reduce the cost and improve the solar cell manufacturing throughput. In situ and real-time spectroscopic ellipsometry (RTSE) has been used conjointly with ex situ characterizations to understand the properties of ultrathin CIGS films. This enables monitoring the growth process, analyzing the optical properties of the CIGS films during deposition, and extracting composition, film thickness, grain size, and surface roughness which can be corroborated with ex situ measurements. The fabricated devices were characterized using current voltage and quantum efficiency measurements and modeled using a 1-dimensional solar cell device simulator. An analysis of the diode parameters indicates that the efficiency of the thinnest cells was restricted not only by limited light absorption, as expected, but also by a low fill factor and open-circuit voltage, explained by an increased series resistance, reverse saturation current, and diode quality factor, associated with an increased trap density.

1. Introduction

$Cu(In,Ga)Se_2$ (CIGS) is one of the most promising materials for obtaining low-cost and high-efficiency thin-film solar cells viable for large-scale production. It is a versatile material that forms a variety of alloys [1–7], deposited by a variety of methods [8–12] and has now attained a maximum power conversion efficiency of 22.6% [13]. Several studies have proven the high efficiency (>18%) and stability of CIGS-based modules [14, 15]. The capacity to scale up any photovoltaic technology is one of the criteria that will determine its long-term viability. In the case of CIGS, many manufacturers are paving the way for GW-scale production capacity. However, as CIGS technology continues to increase its share of the market, the scarcity and high price of indium may potentially affect its ability to compete with other technologies. One way to avoid this bottleneck is to reduce the importance of indium and gallium in the fabrication of the cell simply by reducing CIGS thickness without significant loss in its efficiency. The typical thickness of the CIGS absorber layer is generally about 2–2.5 μm [15, 16]. CIGS has a relatively high absorption coefficient (~10^5 cm^{-1} at 1.4 eV and higher), which can allow 0.5 μm thickness of the CIGS absorber layer to absorb more than 90% of the total incident solar spectrum [16]. The concept of thinning the CIGS layer is therefore of great interest and has already been explored by several researchers [17–19]. As mentioned, the potential advantages of this concept derive from the reduction of cost and usage of materials (especially In and Ga) and the increase in production throughput.

In this study, we focus on the growth process of CIGS films for various thicknesses (1.95 μm to 0.35 μm) characterized by in situ real-time spectroscopic ellipsometry (RTSE), and the results are correlated with ex situ measurements
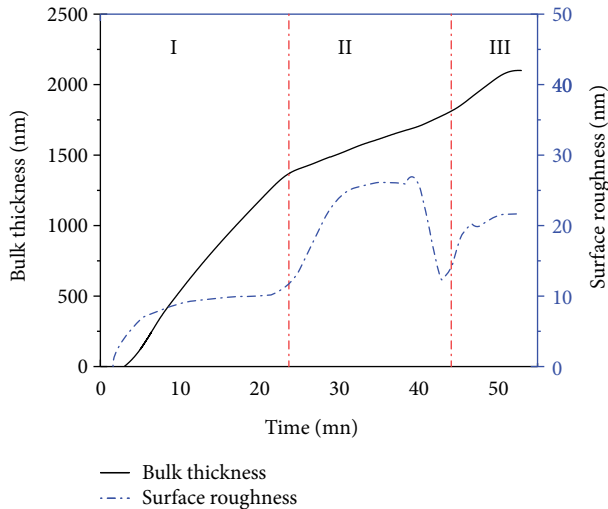
FIGURE 1: Evolution of bulk layer thickness and surface roughness layer thickness—obtained throughout three-stage CIGS growth for $2.0\,\mu$m-thick CIGS layer.

such as XRF, XRD, and SEM. CIGS solar cell devices with different thickness of CIGS layers are fabricated, and their device parameters are correlated with characterization and modeling results.

2. Materials and Methods

CIGS layers were deposited on soda lime glass (SLG) coated with thin film Mo of thickness approximately 800 nm, by a three-stage coevaporation process similar to that used for high-efficiency devices [13]. The substrate temperature was maintained at 400°C during the first stage and was increased to 550°C during the second and third stages. The targeted composition was between 0.8 and 0.9 for Cu/(In + Ga) and between 0.2 and 0.3 for Ga/(In + Ga). Thinning of the CIGS films was achieved by reducing the deposition time, leading to thicknesses ranging from $1.95\,\mu$m to $0.35\,\mu$m.

Real-time spectroscopic ellipsometry (RTSE) measurements were carried out in situ during CIGS thin-film growth using a rotating compensator, multichannel instrument with an energy range of 0.75–6.5 eV at an angle of incidence of 70° IR sensor was used to monitor the substrate temperature. The RTSE methodology used here has been described in detail in previous work [20–24]. Pairs of (ψ, Δ) spectra were collected with a 3-second acquisition time. The optical model for RTSE data analysis is used to obtain the evolution of the structure including the thickness of the bulk layer and surface roughness layer and the void volume percentage in the surface roughness layer. The effective thickness or volume/area of film is defined as the bulk layer thickness plus one-half of the surface roughness layer thickness [25].

The average composition and thickness of each film was measured using X-ray fluorescence (XRF). A reference sample with known composition and thickness was used to calibrate the XRF measurements. Scanning electron

microscopy (SEM) was used to investigate the cross sections of the samples, and the thickness was correlated with XRF measurements. The structural analysis was done by X-ray diffraction (XRD) measurements.

CIGS solar cells were fabricated by depositing CdS by chemical bath deposition on the SLG/Mo/CIGS structure, then i-ZnO and ZnO:Al by RF sputtering. Solar cells were completed by e-beam evaporation of Ni/Al/Ni metal grids. Cells with total area of 0.50 cm^2 were defined by mechanical scribing. Current-voltage (J-V) under an AM1.5 global spectrum at 25°C and quantum efficiency (QE) measurements were performed on these devices.

3. Results and Discussion

3.1. In Situ Growth Analysis. To scale up solar cell processing with thin CIGS for large-area photovoltaic (PV) technology, the challenge is to achieve optimum values of the thickness of the layers as well as to obtain the desired Cu stoichiometry and alloy composition x within narrow ranges and simultaneously over large areas during CIGS film deposition. As a result, contactless metrologies that provide such information in real time are of great interest in this technology, especially for the development of ultra-thin CIGS. We have demonstrated the use of RTSE for real-time monitoring and control of thin-film CIGS deposition [22]. Three sequential deposition processes are executed to obtain the final CIGS film. During the first stage of deposition, In, Ga, and Se are evaporated at relatively low substrate temperature (~400°C). The second stage includes deposition of Cu and Se at high substrate temperature (~550°C). During this stage, the film composition changes from $(In_{1-x}Ga_x)_2Se_3$ to the Cu-rich $Cu(In,Ga)Se_2$ composition through the stoichiometric $Cu(In,Ga)Se_2$ composition. When the CIGS film becomes Cu rich, a semiliquid $Cu_{2-x}Se$ phase is believed to form on the bulk layer which consists of mixed phases of $Cu(In,Ga)Se_2$ and $Cu_{2-x}Se$. Due to the presence of the semiliquid $Cu_{2-x}Se$ phase, growth of large grains is known to occur [22]. During the third stage of deposition, the Cu-rich CIGS film is transformed into a Cu-poor film by the deposition of In, Ga, and Se.

RTSE measurements are sensitive to the monolayer changes, and they provide sensitive information about the evolution of surface roughness, thus revealing grain growth and coalescence processes. The analysis is performed in real time during each CIGS deposition, and structural parameters (d_b, d_s) were extracted. Detailed studies were performed to describe the use of RTSE for analysis of (i) $(In_{1-x}Ga_x)_2Se_3$ (IGS) formation during stage I of the deposition process, (ii) the conversion of IGS into CIGS during stage II and the rapid development of bulk $Cu_{2-x}Se$ during the end of stage II, and (iii) the Cu-rich to Cu-poor CIGS thin-film transition during stage III. RTSE analysis was performed based on the optical models constructed for the stages of growth of the CIGS film. The optical model for stage I analysis includes layers consisting of (i) a Mo/IGS interface roughness layer, having a thickness approximately equal to the surface roughness of the Mo surface; (ii) an IGS bulk layer of thickness d_b; and
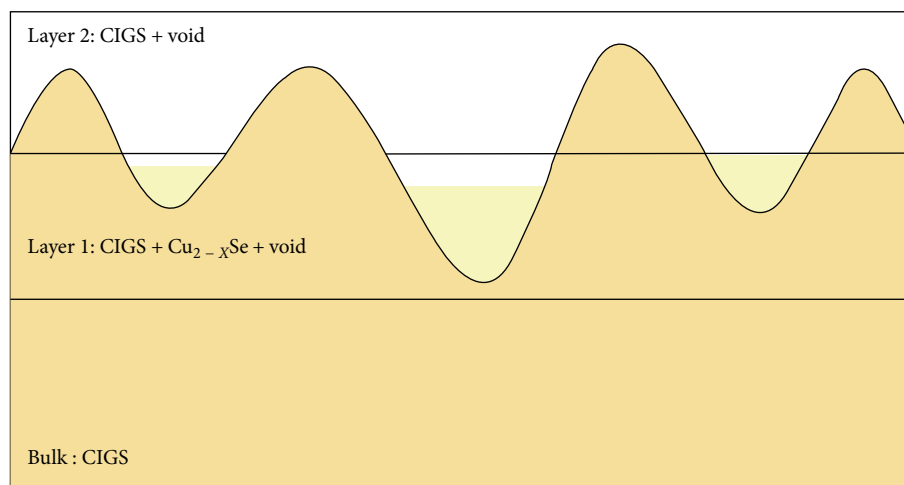
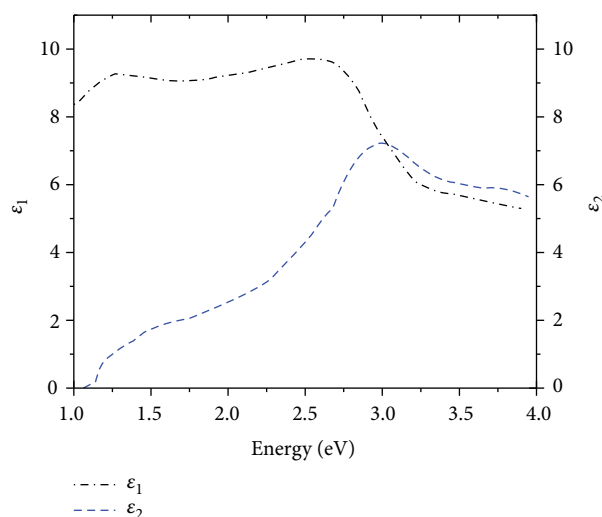FIGURE 2: Optical model for real-time analysis of the third stage of three-stage CIGS deposition.

FIGURE 3: Real and imaginary parts of the dielectric function extracted from RTSE for 0.35 μm ultrathin Cu(In,Ga)Se$_2$ film.

(iii) an IGS surface roughness layer of thickness d_s, whereas the model for stages II and III adds CIGS to the IGS bulk layer and Cu$_{2-x}$Se to the CIGS surface layer.

The time evolution of the bulk thickness and surface roughness (d_b, d_s) for the ~2.0 μm CIGS film is shown in Figure 1. Similar measurements were carried out for all film thicknesses. The Volmer-Weber growth mode is observed, whereby growth occurs through islands, and atoms have a tendency to bind to each other rather than to the substrate.

The surface and interface roughness layers are modeled based on the Bruggeman effective medium approximation (EMA) as a mixture of underlying and overlying materials. During the initial stage of IGS growth (stage I), the voids in the Mo surface roughness are filled by IGS, and this leads to a rapid increase in the IGS layer thickness, leading to a simultaneous increase in the surface roughness of the IGS layer. During initial bulk layer growth, the roughness thickness on the IGS decreases indicating suppression of substrate-induced roughness and apparent coalescence of the islands on the Mo surface. Later, the IGS roughness increases due to crystallites protruding above the surface.

For the initial analysis of stage II, a bulk conversion model is constructed considering that the entire IGS layer is converted into CIGS. In this stage, CIGS nucleates uniformly within the bulk IGS layer, and the grain size and the concentration of grains increase with time at the expense of the surrounding IGS material until the entire IGS layer is consumed. In this process, the bulk layer thickness increases as the Cu is incorporated. Thus, it is assumed that IGS, CIGS, and Cu$_{2-x}$Se components of the bulk layer are resolvable at any time during Cu exposure, and as a result, the film is modeled with a uniform bulk layer according to a three-component Bruggeman EMA. During stage III, the Cu-rich CIGS film is transformed into a Cu-poor film by the deposition of In, Ga, and Se, in order to provide a suitable absorber layer for the CIGS solar cell. An optical model of two surface layers consisting of CIGS surface roughness (associated with crystallites protruding above the surface), as well as an underlying layer consisting of Cu$_{2-x}$Se, CIGS, and voids, was developed to monitor the Cu-rich to Cu-poor transition. With this model, the Cu-rich to Cu-poor transition can be identified as the time at which the Cu$_{2-x}$Se volume fraction (also its effective thickness) decreases to zero which indicates the stoichiometric point. The deposition is terminated after the transition of the Cu-rich CIGS film to Cu-poor film by coevaporating In, Ga, and Se. The optical model used for RTSE analysis for the third stage is shown in Figure 2. The two surface layers describe the roughness as well as the Cu-rich phase at the surface of the film, providing the Cu$_{2-x}$Se content when the film transitions to Cu poor.

The analysis that provides the evolution of the thicknesses (d_b, d_s) in Figure 1 also provides the complex dielectric functions $(\varepsilon_1, \varepsilon_2)$ for the CIGS thin films (Figure 3). The dielectric functions are closely linked to the electronic band structure. The observed features in $(\varepsilon_1, \varepsilon_2)$ in Figure 3 are related to interband transitions that appear at the Van Hove singularities or critical points (CPs) of the joint density of

TABLE 1: Critical point energy (eV) and broadening (eV) extracted from RTSE for 0.35 μm ultrathin Cu(In,Ga)Se$_2$ film.

	$E_0(A, B)$	$E_0(C)$	$E_1(A)$	$E(X\Gamma)$	$E_1(B)$	$E'(X\Gamma)$	$E_2(A)$	E_3	E_4
CP En. (eV)	1.13	1.46	2.71	3.2	3.81	4.16	4.61	5.21	5.50
Γ (eV)	0.32	0.22	0.46	0.31	0.23	0.21	0.21	0.91	0.21

TABLE 2: Thickness, average composition, and average band gap for the CIGS films as obtained by XRF and RTSE measurements.

Thickness (μm)	Cu (at %)	In (at %)	Ga (at %)	Cu/ (In + Ga) (y)	Ga/ (In + Ga) (x)	Average E_g from XRF (eV)	Average E_g from RTSE (eV)
1.95	23.4	20.7	6.3	0.87	0.23	1.12	1.12
1.55	22.4	20.8	6.9	0.81	0.25	1.13	1.13
1.25	22.7	20.1	6.3	0.86	0.24	1.13	1.12
0.75	21.8	21.0	6.3	0.80	0.23	1.12	1.13
0.55	21.0	19.8	6.2	0.81	0.24	1.13	1.13

states. These features were fitted assuming parabolic bands (PBs), yielding CPPB oscillators given by

$$\varepsilon_j(\omega) = \begin{cases} C_j - A_j e^{i\phi_j} \left(\omega - E_j + i\Gamma_j\right)^n, & n = -1, -\frac{1}{2}, +\frac{1}{2}, \\ C_j - A_j e^{i\phi_j} \ln\left(\omega - E_j + i\Gamma_j\right), & n = 0, \end{cases}$$

(1)

where A_j is the amplitude, E_j is the energy, Γ_j is the broadening, and ϕ_j is the phase, all for the jth critical point. The exponent n is -1, $-1/2$, 0 (ln), or $+1/2$ for excitonic, 1-dimensional, 2-dimensional, or 3-dimensional CPs, respectively. Because some CPs were not easily resolved, the second derivatives of the dielectric functions were used in the fitting of the CPPB oscillators, according to the expressions [26]:

$$\frac{d^2\varepsilon(E)}{dE^2} = \sum_n \begin{cases} -A_n e^{i\varphi_n} \mu_n(\mu_n - 1)(E - E_n + i\Gamma_n)^{\mu_n-2}, & \mu_n \neq 0, \\ -A e^{i\varphi_n} (E - E_n + i\Gamma_n)^{-2}, & \mu_n = 0, \end{cases}$$

(2)

where $E = \hbar\omega$ is the photon energy. The remaining four parameters for each CP were obtained in fits to the second derivatives of the dielectric functions obtained as described elsewhere [27]. The CP energies as well as the broadening of the CPs obtained from the fits are compiled in Table 1 for the 0.35 μm film. For the first three transitions, $E_0(A, B)$ and $E_0(C)$, the best fits were obtained with excitonic line shapes; for the rest of the transitions, 2D line shapes were used. The electronic transition assignments in Table 1 follow from a comparison of the room temperature CP energies of the polycrystalline films with those of single crystal [26].

Slight variations in the energy values would likely correspond to variations in the composition for films of different thickness. This was later correlated with ex situ measurements.

The CPs are not only directly useful for determining the band gap, which is a critical parameter for the solar cell, but also potentially useful for distinguishing between two materials with different properties that may lead to different device performance parameters. The broadening parameters for the CIGS films were observed to narrow with the increase in thickness of the film, indicating an increase of the grain size with the increase in thickness.

3.2. Ex Situ Thin Film Characterization. The CIGS films were characterized by XRF for average composition and thickness (Table 2). As one can see, the compositions matched the targeted range. Applying the relationship between the room temperature bandgap ($E_g = E_0$) and the atomic ratio $x = [Ga]/([In] + [Ga])$, given by $E_g = 1.01 + 0.626x - 0.167x(1 - x)$, the average band gap was extracted from the XRF composition for each film and correlated with the average band gap obtained from RTSE. The average composition extracted from XRF is in good agreement with the average composition extracted from RTSE as shown in Table 2. Note that these average values do not allow for the existing composition gradient in the films to be assessed.

The film thicknesses were measured by XRF and by cross-sectional SEM (Figure 4). They were also correlated with the RTSE measurements and demonstrated that the targeted thicknesses were obtained (Table 2).

Figure 5 shows the general XRD patterns for all the CIGS films. All the peaks can be indexed by chalcopyrite polycrystalline Cu(In$_{1-x}$Ga$_x$)Se$_2$ and Mo, which indicates that the CIGS films are single phase. The value of x was varied to match the peak position and correlated well with the values found by XRF.

The preferred orientation for all the films was (220)/(204) while the FWHM increased for the thinner films, in good agreement with the cross-sectional SEM images (Figure 4), indicating smaller grains for the thinner films. The CP broadening parameter (Γ) for the CIGS thin films with different thickness extracted from RTSE (Table 1) also corroborated the same trend as seen in XRD and SEM.

3.3. Device Fabrication and Analysis. J-V and QE results for the devices are reported in Table 3 and Figure 6. One can observe that the short-circuit current and the open-circuit voltage are roughly constant as thickness is reduced from 1.95 μm to 1.25 μm, while decreasing for 0.75 μm down to 0.35 μm. The decrease in current below CIGS thickness of 1.25 μm was confirmed by QE measurements. This effect on the current was expected, as there is a decrease in absorbance at long wavelengths with decreasing CIGS thickness [28]. It was found, however, that the reduction of QE is greater than the reduction of absorbance at the long wavelengths, which can be due to
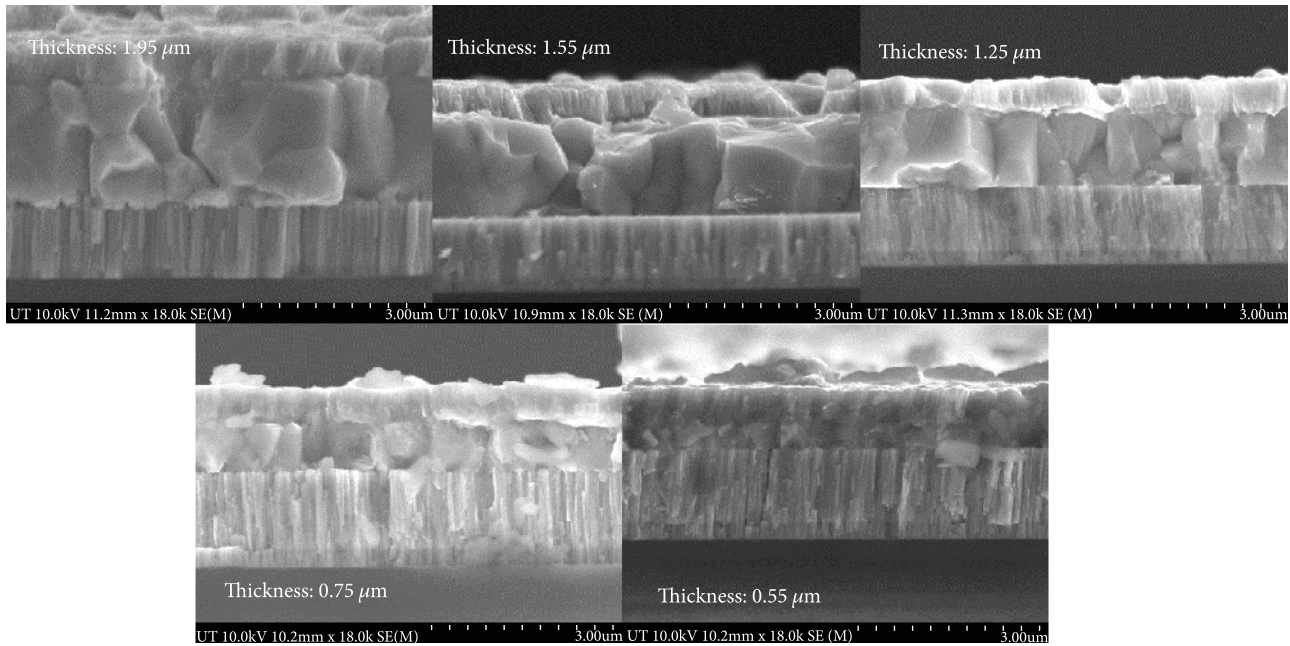
FIGURE 4: Cross-sectional SEM images of the CIGS solar cells with different CIGS thickness deposited by the 3-stage process.
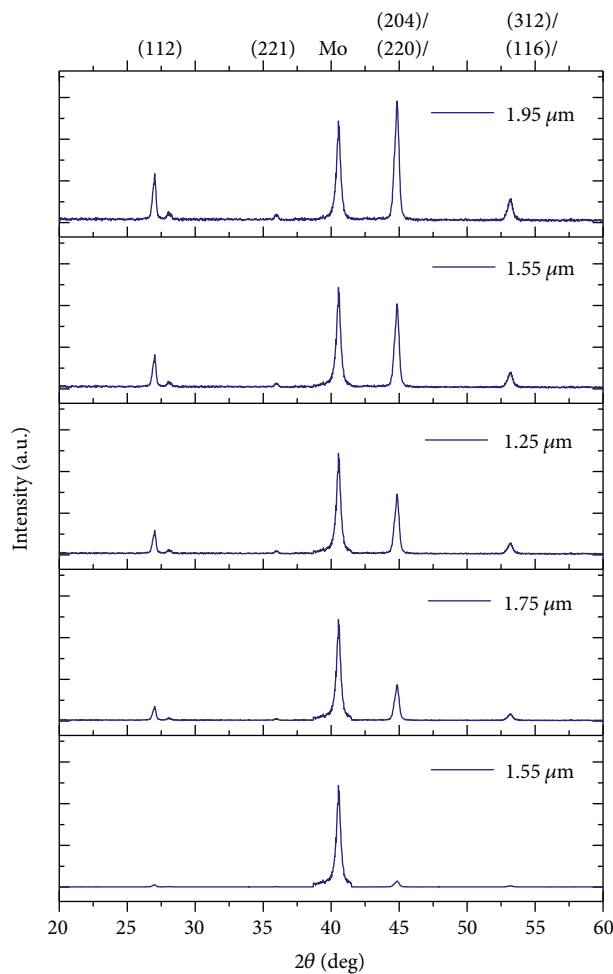

FIGURE 5: XRD patterns as a function of CIGS film thickness.

TABLE 3: Solar cell parameters for CIGS solar cells deposited by 3-stage process with various thicknesses (shunt conductance was low in all cases).

Thickness (μm)	V_{OC} (V)	J_{SC} (mA/ cm^2)	FF (%)	J_0 (mA/ cm^2)	A	R_{S} (ohm/ cm^2)	Efficiency (%)
1.95	0.63	35.1	74.6	2.0E-6	1.51	0.8	16.6
1.55	0.63	34.3	72.4	1.0E-5	1.63	0.75	15.4
1.25	0.62	34.3	72.2	1.0E-5	1.55	0.75	15.4
0.75	0.55	32.4	70.8	4.0E-5	1.59	1.2	13.2
0.55	0.52	30.9	63.5	6.0E-4	1.89	2.0	10.2
0.35	0.50	28.1	61.2	4.3E-3	2.16	2.0	8.6

electrical loss mechanisms such as an increase of the series resistance and recombination of photophotogenerated carriers near the back contact [29].

The J-V data were then analyzed using the ideal diode equation considering that the forward diode current is limited by Shockley-Read-Hall (SRH) recombination through the subbandgap energy states within the space charge region (SCR) of the Cu(In,Ga)Se$_2$. The diode equation is given as

$$J = J_0 \exp\left(\frac{q(V - R_s J)}{AkT}\right) - J_0 - J_L + GV, \quad (4)$$

where J_0 is the reverse saturation current density, A is the diode quality factor, R_S is the series resistance, J_L is the light
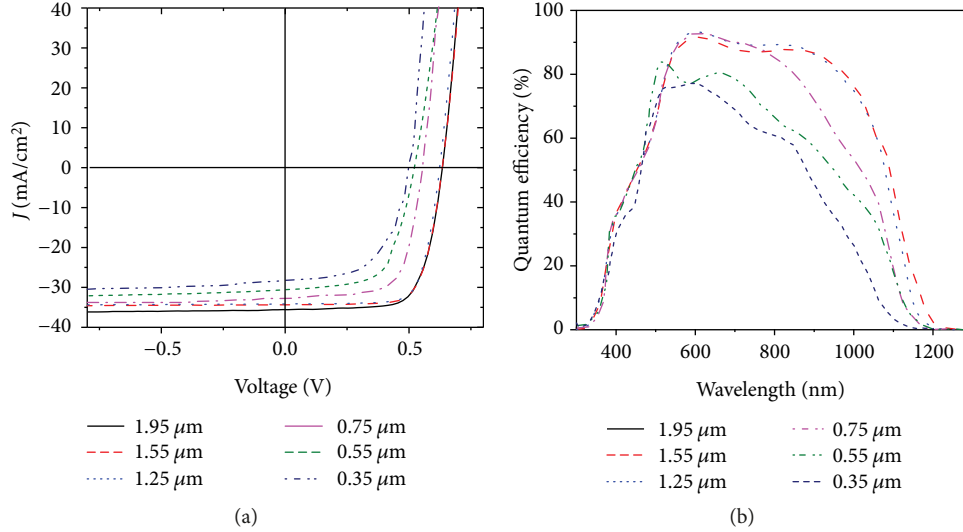
FIGURE 6: J-V measurements and quantum efficiency (QE) of devices fabricated by 3-stage process from Cu(In,Ga)Se$_2$ thin films with different thickness.

TABLE 4: CIGS baseline parameters used for simulations.

(a)

General device properties	Front	Back
Φ_b (eV)	$\Phi_{bn} = 0$	$\Phi_{bp} = 0.2$
S_e (cm/s)	10^7	10^7
S_h (cm/s)	10^7	10^7
Reflectivity	0.05	0.8

(b)

Layer properties	AZO	ZnO	CdS	CIGS
T (nm)	300	200	50	350–1950
$\varepsilon/\varepsilon_o$	9	9	10	13.6
μ_e (cm^2/Vs)	100	100	100	100
μ_h (cm^2/Vs)	25	25	25	25
$N_{D/A}$ (cm^{-3})	N_D: 10^{18}	N_D: 10^{18}	N_D: 10^{18}	N_A: 10^{16}
E_g (eV)	3.3	3.3	2.4	1.15
N_C (cm^{-3})	2.2×10^{18}	2.2×10^{18}	2.2×10^{18}	2.2×10^{18}
N_V (cm^{-3})	1.8×10^{19}	1.8×10^{19}	1.8×10^{19}	1.8×10^{19}

generated current, and G is the shunt conductance. In all cases, the shunt conductance was low. The derived R_S and A, from the intercept and slope, respectively, in a linear fit to dV/dJ plotted versus $(J + J_{sc})^{-1}$ are shown in Table 3.

The higher value for the diode quality factor as the thickness is reduced appears to indicate that the main recombination mechanism is more closely related to interface recombination than to space charge region recombination. The higher value of the series resistance for the thinnest CIGS devices could be one of the reasons for the lower fill factors. The decrease in V_{OC} as absorber layer thinned down below

1 μm could be due to the increase in defect density with the reduction in CIGS absorber layer thickness, as indicated by the increase in reverse saturation current density J_0.

3.4. Device Simulation. In this work, SCAPS software [30] was used for the solar cell simulation. The standard thickness of the CIGS absorber layer is about 2 μm. CIGS absorber layers with various thicknesses, varying from 1.95 μm to 0.35 μm, were incorporated into the numerical simulation. The starting parameters for the simulation model are listed in Table 4. The results of the experimental data as well as the simulations for a bulk trap density of 5×10^{11} cm^{-3} are reported in Figure 7. We observed that all of the electrical parameters (J_{sc}, V_{oc}, FF, and efficiency) decreased for thicknesses below 1 μm. The short-circuit current density (J_{sc}) was the most affected due to the increasing transparency of the thin CIGS layers and due to the recombination at the interface between the absorber layer and the back contact [31]. For ultrathin absorber layers, long wavelengths penetrate deeply into the absorber and generate electron-hole pairs near the back contact, which is the critical region for recombination, resulting in the decrease of V_{oc} and the FF.

The reduction in thickness itself, however, was not sufficient to obtain good agreement between our experimental results and simulations for the ultrathin devices. We also had to introduce a variation in the bulk defect density to allow for a better fit. As we mentioned earlier, in the simulation, the grain boundary recombination has been considered in terms of an increased bulk defect density. Attempts were therefore made to compare the simulation results with our experimental results by introducing an intentionally higher defect density into the absorber layers, as shown in Table 5. Very good agreement was obtained between the simulated solar cell parameters (V_{oc}, J_{sc}, FF, and efficiency) and the experimental results. This requires that the defect density increase from 5×10^{11} cm^{-3} for the 1.95 μm film to 1.6×10^{15} cm^{-3} for the 0.35 μm film. This can be related to the observations made on the films, specifically in terms of
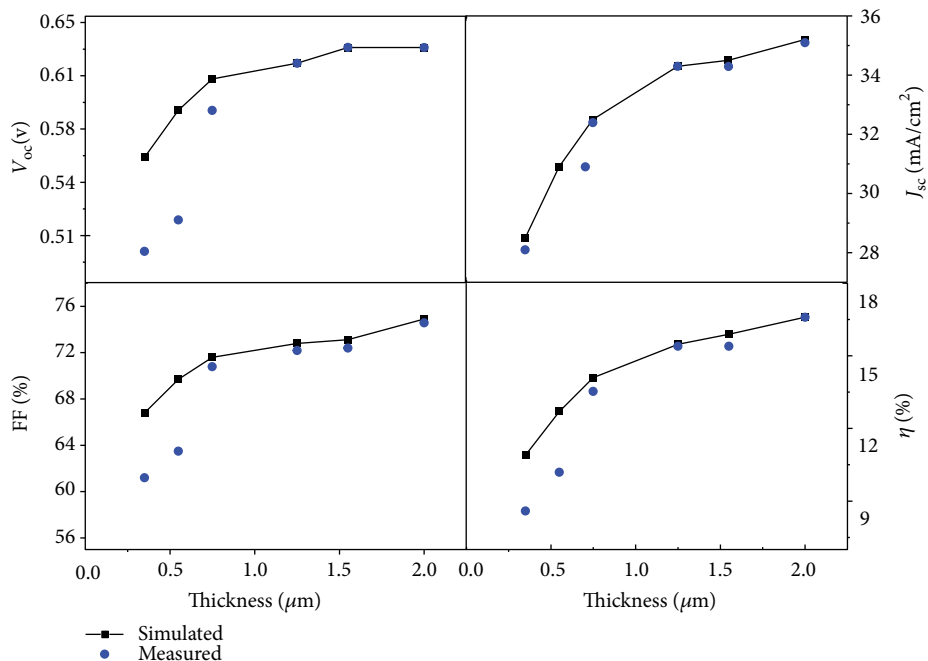
FIGURE 7: Simulated results on the effect of CIGS absorber layer thickness on the short-circuit current density (J_{sc}), open-circuit voltage (V_{oc}), fill factor (FF), and the efficiency for a fixed defect density of 5×10^{11} cm^{-3} (the blue dots indicate measured values).

TABLE 5: Results from the simulation for CIGS solar cells with different thicknesses and with different defect density (the experimental results are in parentheses for comparison).

Thickness (μm)	V_{oc} (V)	J_{sc} (mA/cm^2)	FF (%)	Eff (%)	Defect density (cm^{-3})
		Simulated data (measured data)			
1.95	0.63 (0.63)	35.2 (35.1)	74.9 (74.6)	16.7 (16.6)	5×10^{11}
1.55	0.63 (0.63)	34.5 (34.3)	73.1 (72.4)	15.9 (15.4)	5×10^{11}
1.25	0.62 (0.62)	34.3 (34.3)	72.8 (72.2)	15.5 (15.4)	5×10^{11}
0.75	0.58 (0.55)	32.4 (32.4)	70.8 (70.8)	13.5 (13.2)	1.5×10^{14}
0.55	0.52 (0.52)	30.9 (30.9)	63.7 (63.5)	10.2 (10.2)	9.5×10^{14}
0.35	0.50 (0.50)	29.6 (28.1)	61.7 (61.2)	9.1 (8.6)	1.6×10^{15}

the growth observed by RTSE. For the thinner films, the grain size is effectively smaller and the onset of coalescence of IGS occurs at a time much closer to the end of the deposition of this layer, giving rise to higher bulk defect density.

4. Conclusions

CIGS thin films with various thicknesses were studied by RTSE and ex situ measurements. All films with different thicknesses exhibit a Volmer-Weber (V-W) growth mode, as observed by RTSE. The grain size decreases as the thickness of the absorber layer decreases from 1.95 μm to 0.35 μm. XRD spectra revealed (220)/(204) preferred orientation for these films. Consistent results were obtained for the composition, band gap, thickness, and grain size by RTSE, XRD, SEM, and XRF. The solar cells were then characterized by current voltage and quantum efficiency measurements. As expected, the current density decreases as the thickness of the absorber layer decreases. However, the other device parameters (V_{OC}, FF) also decrease. The diode parameter analysis of the

studied CIGS solar cell devices indicates that the thinnest cells are limited in efficiency by a low fill factor and open-circuit voltage, associated primarily with a high diode quality factor ($A = 2.16$), high series resistance ($R_S \sim 2\Omega$ cm^2) and high reverse saturation current density ($J_0 = 4.3 \times 10^{-3}$ mA/cm^2). SCAPS simulations indicate that a trap density of 5×10^{11} cm^{-3} is appropriate to simulate the higher thicknesses but that a higher trap density, up to 1.6×10^{15} cm^{-3}, is necessary to obtain good agreement with the results for the ultrathin layers (0.35 μm).
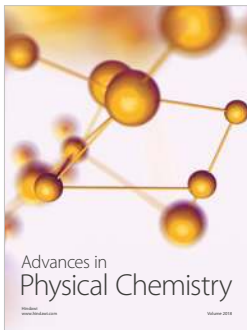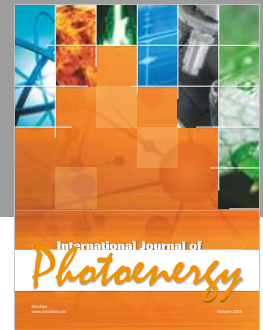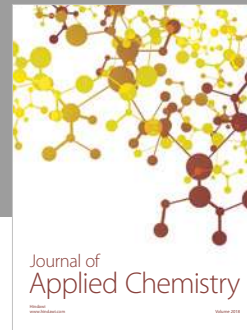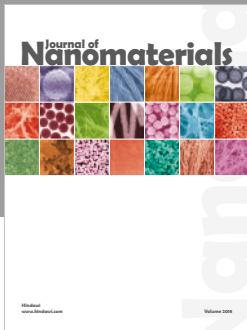
Conflicts of Interest

The authors declare that there is no conflict of interest regarding the publication of this paper.

References

[1] P. D. Paulson, M. W. Haimbodi, S. Marsillac, R. W. Birkmire, and W. N. Shafarman, "CuIn$_{1-x}$Al$_x$Se$_2$ thin films and solar

cells," *Journal of Applied Physics*, vol. 91, no. 12, pp. 10153–10156, 2002.

[2] S. Marsillac, M. C. Zouaghi, J. C. Bernede, T. Ben Nasrallah, and S. Belgacem, "Evolution of the properties of spray-deposited $CuInS_2$ thin films with post-annealing treatment," *Solar Energy Materials and Solar Cells*, vol. 76, no. 2, pp. 125–134, 2003.

[3] S. A. Little, V. Ranjan, R. W. Collins, and S. Marsillac, "Growth analysis of $(Ag,Cu)InSe_2$ thin films via real time spectroscopic ellipsometry," *Applied Physics Letters*, vol. 101, no. 23, article 231910, 2012.

[4] S. Marsillac, P. D. Paulson, M. W. Haimbodi, R. W. Birkmire, and W. N. Shafarman, "High-efficiency solar cells based on $Cu(InAl)Se_2$ thin films," *Applied Physics Letters*, vol. 81, no. 7, pp. 1350–1352, 2002.

[5] E. Halgand, J. C. Bernède, S. Marsillac, and J. Kessler, "Physico-chemical characterisation of $Cu(In,Al)Se_2$ thin film for solar cells obtained by a selenisation process," *Thin Solid Films*, vol. 480-481, pp. 443–446, 2005.

[6] S. Marsillac, H. Khatri, K. Aryal, and R. W. Collins, "Properties of $Cu(In,Ga)Se_2$ thin films and solar cells deposited by hybrid process," *International Journal of Photoenergy*, vol. 2012, Article ID 385185, 6 pages, 2012.

[7] L. Stolt, J. Hedström, J. Kessler, M. Ruckh, K. O. Velthaus, and H. W. Schock, "$ZnO/CdS/CuInSe_2$ thin-film solar cells with improved performance," *Applied Physics Letters*, vol. 62, no. 6, pp. 597–599, 1993.

[8] C. Amory, J. C. Bernède, E. Halgand, and S. Marsillac, "$Cu(In,Ga)Se_2$ films obtained from γ-In_2Se_3 thin film," *Thin Solid Films*, vol. 431-432, pp. 22–25, 2003.

[9] C. O. El Moctar, K. Kambas, S. Marsillac, A. Anagnostopoulos, J. C. Bernède, and K. Benchouck, "Optical properties of $CuAlX_2$ (X=Se, Te) thin films obtained by annealing of copper, aluminum and chalcogen layers sequentially deposited," *Thin Solid Films*, vol. 371, no. 1-2, pp. 195–200, 2000.

[10] M. C. Zouaghi, T. B. Nasrallah, S. Marsillac, J. C. Bernède, and S. Belgacem, "Physico-chemical characterization of spray-deposited $CuInS_2$ thin films," *Thin Solid Films*, vol. 382, no. 1-2, pp. 39–46, 2001.

[11] C. O. El Moctar, S. Marsillac, J. C. Bernède, A. Conan, K. Benchouk, and A. Khelil, "Preparation of thin CuAlSe2 films by annealing of stacked Cu/Al/Se/Al... layers, study of deposition conditions," *Physica Status Solidi a-Applied Research*, vol. 174, no. 1, pp. 213–220, 1999.

[12] W. Chen, W. Cao, T. A. Hameed, S. Marsillac, and H. E. Elsayed-Ali, "Properties of $Cu(In,Ga,Al)Se_2$ thin films fabricated by pulsed laser deposition," *Journal of Materials Science: Materials in Electronics*, vol. 26, no. 3, pp. 1743–1747, 2015.

[13] P. Jackson, R. Wuerz, D. Hariskos, E. Lotter, W. Witte, and M. Powalla, "Effects of heavy alkali elements in $Cu(In,Ga)Se_2$ solar cells with efficiencies up to 22.6%," *physica status solidi (RRL) - Rapid Research Letters*, vol. 10, no. 8, pp. 583–586, 2016.

[14] A. A. Rockett, "Current status and opportunities in chalcopyrite solar cells," *Current Opinion in Solid State and Materials Science*, vol. 14, no. 6, pp. 143–148, 2010.

[15] V. Probst, W. Stetter, W. Riedl et al., "Rapid CIS-process for high efficiency PV-modules: development towards large area processing," *Thin Solid Films*, vol. 387, no. 1-2, pp. 262–267, 2001.

[16] V. S. Saji, I.-H. Choi, and C.-W. Lee, "Progress in electrodeposited absorber layer for $CuIn_{(1-x)}Ga_xSe_2$ (CIGS) solar cells," *Solar Energy*, vol. 85, no. 11, pp. 2666–2678, 2011.

[17] K. Orgassa, H. W. Schock, and J. Werner, "Alternative back contact materials for thin film $Cu(In,Ga)Se_2$ solar cells," *Thin Solid Films*, vol. 431-432, pp. 387–391, 2003.

[18] O. Lundberg, M. Bodegård, J. Malmström, and L. Stolt, "Influence of the $Cu(In,Ga)Se_2$ thickness and Ga grading on solar cell performance," *Progress in Photovoltaics: Research and Applications*, vol. 11, no. 2, pp. 77–88, 2003.

[19] K. Ramanathan, R. Noufi, B. To et al., "Processing and properties of sub-micron CIGS solar cells," in *2006 IEEE 4th World Conference on Photovoltaic Energy Conference*, pp. 380–383, Waikoloa, HI, USA, 2006, IEEE.

[20] K. Aryal, G. Rajan, T. Ashrafee et al., "Effect of selenium evaporation rate on ultrathin Cu(In,Ga)Se2 films," in *2014 IEEE 40th Photovoltaic Specialist Conference (PVSC)*, pp. 0314–0317, Denver, CO, USA, 2014, IEEE.

[21] K. Aryal, H. Khatri, R. W. Collins, and S. Marsillac, "In situ and ex situ studies of molybdenum thin films deposited by rf and dc magnetron sputtering as a back contact for CIGS solar cells," *International Journal of Photoenergy*, vol. 2012, Article ID 723714, 7 pages, 2012.

[22] V. Ranjan, T. Begou, S. Little, R. W. Collins, and S. Marsillac, "Non-destructive optical analysis of band gap profile, crystalline phase, and grain size for $Cu(In,Ga)Se_2$ solar cells deposited by 1-stage, 2-stage, and 3-stage co-evaporation," *Progress in Photovoltaics: Research and Applications*, vol. 22, no. 1, pp. 77–82, 2014.

[23] T. Begou, J. D. Walker, D. Attygalle, V. Ranjan, R. W. Collins, and S. Marsillac, "Real time spectroscopic ellipsometry of $CuInSe_2$: growth dynamics, dielectric function, and its dependence on temperature," *physica status solidi (RRL) - Rapid Research Letters*, vol. 5, no. 7, pp. 217–219, 2011.

[24] V. Ranjan, R. W. Collins, and S. Marsillac, "Real-time analysis of the microstructural evolution and optical properties of $Cu(In,Ga)Se_2$ thin films as a function of Cu content," *physica status solidi (RRL) - Rapid Research Letters*, vol. 6, no. 1, pp. 10–12, 2012.

[25] H. V. Nguyen, I. An, and R. W. Collins, "Evolution of the optical functions of thin-film aluminum: a real-time spectroscopic ellipsometry study," *Physical Review B*, vol. 47, no. 7, pp. 3947–3965, 1993.

[26] M. I. Alonso, K. Wakita, J. Pascual, M. Garriga, and N. Yamamoto, "Optical functions and electronic structure of $CuInSe_2$, $CuGaSe_2$, $CuInS_2$, and $CuGaS_2$," *Physical Review B*, vol. 63, no. 7, article 075203, 2001.

[27] P. Lautenschlager, M. Garriga, and M. Cardona, "Temperature dependence of the interband critical-point parameters of InP," *Physical Review B*, vol. 36, no. 9, pp. 4813–4820, 1987.

[28] A. Han, Y. Zhang, W. Song, B. Li, W. Liu, and Y. Sun, "Structure, morphology and properties of thinned $Cu(In, Ga)Se_2$ films and solar cells," *Semiconductor Science and Technology*, vol. 27, no. 3, article 035022, 2012.

[29] P. Jackson, D. Hariskos, E. Lotter et al., "New world record efficiency for $Cu(In,Ga)Se_2$ thin-film solar cells beyond 20%," *Progress in Photovoltaics: Research and Applications*, vol. 19, no. 7, pp. 894–897, 2011.

[30] S. Degrave, M. Burgelman, and P. Nollet, "Modelling of poly-crystalline thin film solar cells: new features in scaps version 2.3," in *Proceedings of 3rd World Conference onPhotovoltaic Energy Conversion, 2003*, pp. 487–490, Osaka, Japan, 2003, IEEE.

[31] Z. Jehl, F. Erfurth, N. Naghavi et al., "Thinning of CIGS solar cells: part II: cell characterizations," *Thin Solid Films*, vol. 519, no. 21, pp. 7212–7215, 2011.